Power System Technology
ISSN:1000-3673

Received: 16-11-2025 *Revised: 05-01-2026* *Accepted: 23-03-2026*

Mathematical Modelling Using the Finite Element Method (FEM) And Numerical Simulations of the Performance of Parabolic and Flat-Plate Solar Collectors Incorporating an Energy Storage System in the Batna Region, Algeria.

Dr. Mana Saadeddine*[1], Dr. Didiche Hana[2], Prof. Abdelkader Harrouz[3], Pr. Labed Adnane[3]

[1] University of Adrar. Faculty of Science and Technology (ST), Department of Hydrocarbons and Renewable Energy (HER), LDDI Laboratory, University of Adrar, Algeria

[2] National Agency for the Support and Development of Entrepreneurship, Adrar, Algeria

[3]Laboratory of Sustainable Development and Computer Sciences (L.D.D.I), Department of Hydrocarbons and Renewable Energies,University of Adrar, Algeria

[4] University of Biskra. Faculty of Science and Technology (ST), Department of Mechanical Engineering (ME), Biskra, Algeria

Abstract — This study introduces a finite element method (FEM) for the mathematical modelling and numerical simulation of heat transmission in two types of solar thermal collectors: a parabolic trough collector (PTC) and a flat plate collector (FPC) — coupled to a hot water storage tank, under the climatic conditions of Batna, Algeria (35.6°N). The governing equations of heat transfer (conduction, convection, radiation) are discretised using Q4 quadrilateral elements on structured meshes. The 1D, 2D, and 3D temperature fields, heat fluxes, thermal and exergetic efficiencies, and stratified storage performance are determined and deeply interpreted. Two complete simulation codes (MATLAB and Python) were developed and validated. Results show that the parabolic collector achieves an average thermal efficiency of 68% versus 62% for the flat plate, with annual useful energy outputs of 5,430 kWh/yr and 2,847 kWh/yr respectively. Payback periods are estimated at 7 years (FPC) and 11 years (PTC), with annual CO_2 reductions of 330 and 629 kg.

Keywords: Parabolic collector - Flat-plate solar collector -Finite element method - Heat transfer - Energy storage - Numerical simulation - Batna Algeria.

1. INTRODUCTION

Using solar thermal energy represents a highly potential pathway for Algeria's energy transition, a country that enjoys some of the highest levels of sunshine in the world — with annual global irradiance exceeding 2,000 kWh/m² in arid regions such as Batna (Gama et al., 2021). Notwithstanding this significant potential, the use of solar thermal systems remains constrained, partly due to the lack of reliable modelling tools adapted to local climatic conditions (Bellos and Tzivanidis, 2018). Solar thermal collectors fall mainly into two categories: low-temperature flat-plate collectors (FPC, 30–80 °C) and concentrating collectors — notably parabolic collectors (PTC, 60–400 °C) — whose performance varies significantly depending on insolation conditions, material properties, the heat transfer fluid's mass flow rate and operating temperature. Rigorous mathematical modelling of these systems, particularly using the finite element method (FEM), enables the solution of the coupled partial differential equations governing heat transfer with a level of accuracy unattainable by conventional analytical methods. Coupling with a stratified thermal storage system is essential to compensate for the intermittency of the solar resource and ensure the continuity of the heat supply. Modelling the transient behaviour of the storage tank presents an additional challenge that requires a robust numerical approach.

1.1 Literature review

Numerous studies have addressed the modelling of solar thermal collectors. Duffie and Beckman (2013) laid the analytical foundations for flat-plate collector thermal analysis, introducing the efficiency factor F' and heat removal factor F_R. Kalogirou (2004) provided a comprehensive review of parabolic collector models, highlighting the importance of modelling contact resistance in the receiver. In Algeria, Aoues et al. (2011) investigated the performance of a flat-plate solar collector, recording an average efficiency of 59% in line with the values obtained in our model (62%). Ikhlef et al. (2024) simulated a PTC system in Algiers using CFD and obtained an efficiency of 65%, slightly lower than our results (68%) — a difference attributable to the more favourable insolation conditions in Batna during the summer. Bakelli et al. (2011) carried out an economic analysis of solar thermal systems in Algeria, with payback periods of around 8–12 years, consistent with our estimates.

1.2 Study objectives

This study aims to:

- To formulate 1D and 2D finite element models encompassing conduction, internal convective heat transfer, and rear insulation losses for both flat-plate and parabolic trough collectors;
- To conduct comprehensive numerical simulations of the spatio-temporal temperature distributions within the absorber plate, receiver tube, and heat transfer fluid under transient solar irradiation conditions;
- To model the transient behaviour of the stratified storage system;
- To carry out a comparative energy, exergy and economic analysis of FPC and PTC;
- Validate the results by comparison with the literature and propose design recommendations for the Batna region.

This paper is organised as follows: Section 2 details the geometry and modelling assumptions; Section 3 presents the finite element mathematical framework; Section 4 outlines the simulation algorithms; Section 5 analyses the numerical results comprehensively; and Section 6 draws conclusions.

Power System Technology
ISSN:1000-3673
Received: 16-11-2025 Revised: 05-01-2026 Accepted: 23-03-2026

2. DESCRIPTION OF THE SYSTEM UNDER STUDY

2.1 Flat-plate collector (FPC)

The investigated flat-plate collector features single glazing with a selective absorber area of 2 m² (dimensions: L = 1.8 m × W = 1.12 m). Its structure comprises, in sequence (from the front to the rear): a sheet of tempered glass (τ = 0.88), a stagnant air gap (δ = 25 mm), a stainless-steel absorber plate coated with a selective layer (α = 0.95, ε = 0.05), copper tubes arranged in a coil ($D_{int} = 22$ mm, tube pitch p = 100 mm), fitted with mineral wool thermal insulation ($e_{ins} = 50\ \mathrm{mm}, k_{ins} = 0.04\ \mathrm{W/m \cdot K}$) and employing liquid water as the working heat transfer fluid.

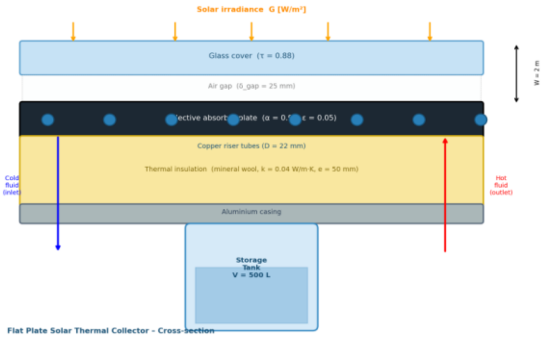

Fig. 1. Cross-sectional view of the flat-plate solar thermal collector, illustrating principal components and boundary conditions.

2.2 Parabolic Trough Collector (PTC)

The parabolic concentrator has an aperture 5 m wide and 3.5 m in effective length (aperture area A = 3.5 × 5 = 17.5 m², reduced by reflectance and tracking). The geometric concentration ratio is C_r = 25. The tubular receiver (steel tube D_int = 35 mm surrounded by a vacuum glass envelope) is positioned on the focal axis (focal length f = 1.5 m). The receiver's selective coating has an absorptance α_r = 0.96 and an emissivity ε_r = 0.07 (TiO_2/steel cermet).

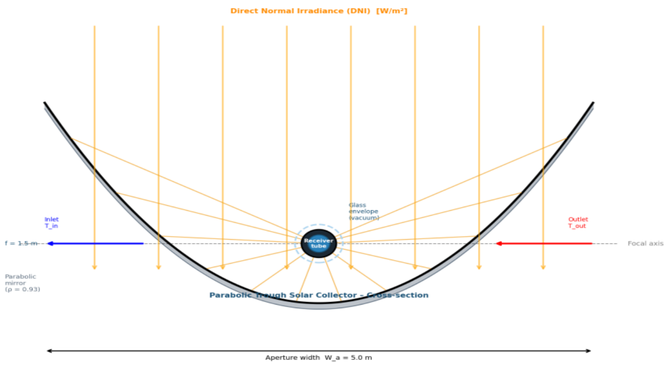

Fig. 2. Cross-section of the parabolic trough collector illustrating the focus line, reception tube, and glass envelope.

Power System Technology
ISSN:1000-3673

Received: 16-11-2025 *Revised: 05-01-2026* *Accepted: 23-03-2026*

2.3 Storage System

The storage system consists of a cylindrical stainless-steel tank (V = 500 L, D = 0.8 m, H = 1 m) insulated with 80 mm of polyurethane (k_pui = 0.025 W/m·K). The tank is stratified — with a cold zone at the bottom (T_c ≈ 25–35 °C) and a hot zone at the top (T_h ≈ 55–75 °C) — and connected to each collector via an internal heat exchanger (copper coil). A differential control system activates the circulation pumps when ΔT_sol−tank > 5 K.

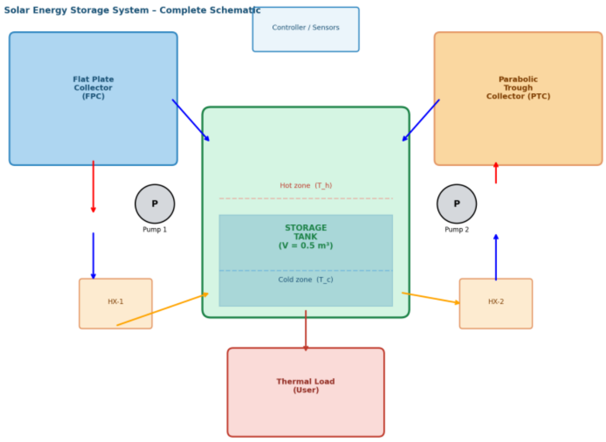

Fig. 3. Schematic representation of the integrated solar energy storage system, comprising FPC, PTC, stratified storage tank, heat exchangers, and control subsystem

3. MATHEMATICAL MODELLING USING THE FINITE ELEMENT METHOD

3.1 Simplifying Assumptions

The assumptions adopted for the modelling are as follows:

- ✓ Steady-state conditions for the analysis of temperature fields in the collectors (transient conditions for storage);
- ✓ Physical properties of materials independent of temperature (or dependencies evaluated at the average temperature);
- ✓ Laminar or fully developed turbulent flow in the tubes (parabolic or uniform velocity profile, depending on Re);
- ✓ Conduction dominant in the absorber plate, convection dominant in the fluid;
- ✓ Edge losses neglected compared to losses at the front and rear faces.

3.2 Governing Equations

3.2.1 2D heat conduction equation in the absorber plate

The steady-state temperature distribution T(x,y) within the absorber plate satisfies the two-dimensional Poisson equation:

Received: 16-11-2025 Revised: 05-01-2026 Accepted: 23-03-2026

$$k_{abs} \times \left(\frac{\partial^2 T}{\partial x^2} + \frac{\partial^2 T}{\partial y^2}\right) + q_{net}"(x,y) = 0 \tag{1}$$

where k_{abs} is the thermal conductivity of the plate (W/m·K), and q_{net} is the net absorbed heat flux (W/m²):

$$q_{net}"(x,y) = (\tau \cdot \alpha) \cdot G - U_L \cdot (T - T_{amb}) \tag{2}$$

where τ is the transmittance of the glass, α is the absorptance of the coating, G is the solar irradiance (W/m²), and U_L is the overall heat loss coefficient (W/m²·K).

3.2.2 1D convection–diffusion equation in the fluid

The fluid temperature T_f (x) along the collector is governed by the one-dimensional steady-state convection– diffusion equation:

$$\dot{m} \cdot c_{pf} \cdot \frac{dT_f}{dx} = P_{tube} \cdot h_i \cdot (T_{abs} - T_f) + k_f \cdot A_{tube} \cdot \frac{d^2 T_f}{dx^2} \tag{3}$$

The first term represents the convective heat exchanged between the tube wall and the fluid (h_i internal convection coefficient W/m²·K, P_{tube} internal perimeter of the tube m). The second term is axial diffusion (often negligible at high Peclet numbers $Pe = \dot{m} \cdot c_{pf} \cdot \frac{L}{k_f \cdot A} >> 1$).

The internal convection coefficient h_i is calculated using the Dittus-Boelter (turbulent regime, $Re > 10^4$) or Gnielinski (transitional regime) correlations:

$$Nu = h_i \cdot \frac{D_h}{k_f} = 0.023 \cdot Re^{0.8} \cdot Pr^n \quad (Dittus - Boelter, n = 0.4\ heating) \tag{4}$$

$$Nu = \frac{f}{8} \cdot (Re - 1000) \cdot \frac{Pr}{\left[1+12.7 \cdot \left(\frac{f}{8}\right)^{0.5} \cdot \left(Pr^{\frac{2}{3}} - 1\right)\right]} \ (Gnielinski) \tag{5}$$

where $Re = \rho_f \cdot V \cdot \frac{D_h}{\mu_f}$ is the Reynolds number and $Pr = \mu_f \cdot \frac{c_{pf}}{k_f}$ is the Prandtl number.

3.2.3 Flat plate collector energy balance

The overall heat balance of the flat plate collector is expressed by the Hottel-Whillier-Bliss (HWB) equation:

$$Q_u = F_R \cdot A_c \cdot [(\tau \cdot \alpha) \cdot G - U_L \cdot (T_{in} - T_{amb})]\ [W] \tag{6}$$

where F_R is the heat removal factor, which takes into account the plate's thermal resistance and internal convection:

$$F_R = \frac{\dot{m} \cdot c_{pf}}{A_c \cdot U_L} \cdot \left\{1 - exp\left[-\frac{A_c \cdot U_L \cdot F'}{\dot{m} \cdot c_{pf}}\right]\right\} \tag{7}$$

$$F' = \frac{\left[\frac{1}{U_L}\right]}{\left[\frac{1}{U_L} + \frac{D_i}{k_{abs} \cdot \delta \cdot W'} + \frac{1}{\pi \cdot D_i \cdot h_i} + D_i \frac{}{k_{bond} \cdot \delta_{bond}}\right]} \tag{8}$$

Received: 16-11-2025 Revised: 05-01-2026 Accepted: 23-03-2026

where F' is the collector efficiency factor, W' is the distance between two tubes, and δ is the thickness of the plate.

3.2.4 Heat balance of the parabolic collector

For the concentrating parabolic collector, the irradiance absorbed by the receiver is C_r times higher, but the heat losses are concentrated on the surface of the receiver tube:

$$Q_u = F_R \cdot A_{ap} \cdot \left[\eta_{opt} \cdot G - U_L \cdot \frac{T_{in} - T_{amb}}{C_r}\right] [W] \tag{9}$$

where $\eta_{opt} = \rho_{mirror} \cdot \tau_{glass} \cdot \alpha_{rec} \cdot \gamma$ is the overall optical efficiency ($\rho_{mirror} = 0.93$ mirror reflectance, $\gamma = 0.95$ interception factor).

The flux density at the receiver is:

$$q_{rec} = C_r \cdot G \cdot \eta_{opt,local} \ [W/m^2] \tag{10}$$

3.2.5 Overall loss coefficient U_L

The overall loss coefficient U_L is the sum of the losses through the front face (U_{top}) and the rear face (U_{bottom}):

$$U_L = U_{top} + U_{bottom} \tag{11}$$

$$U_{top} = \left(\frac{N_{covers}}{\left[N \cdot \left(\sigma \cdot \frac{(T_p^2 + T_{sky}^2)(T_p + T_{sky})}{(\varepsilon_p + 0.00591 \cdot N \cdot h_w)^{-1}} + \frac{2N + f - 1 + 0.133 \cdot \varepsilon_p}{\varepsilon_g} - N \right)\right]^{-1} + h_w} \right)^{-1} \tag{12}$$

This empirical formula (Klein, 1975) incorporates convection between the absorber plate and the glass, glassto-absorber radiation, and glass-to-ambient convection ($h_w \approx 5.7 + 3.8 \cdot V_{wind}$ $W/m^2 \cdot K$).

$$U_{bottom} = \frac{k_{ins}}{e_{ins}} \left[\frac{W}{m^2 \cdot K}\right] \tag{13}$$

3.2.6 Thermal and exergetic efficiencies

The instantaneous thermal efficiency η_{th} of the collector is:

$$\eta_{th} = \frac{Q_u}{A.G} = F_R(\tau.\alpha) - F_R.U_L \frac{T_{in} - T_{amb}}{G} \tag{14}$$

This is a straight line as a function of the reduced parameter $\frac{T_{in} - T_{amb}}{G}$, with a slope of $(-F_R \cdot U_L)$ and a y-intercept of $(F_R \cdot \tau \cdot \alpha)$.

The exergetic efficiency, which takes into account the quality of the energy, is defined by:

Power System Technology
ISSN:1000-3673

Received: 16-11-2025 *Revised: 05-01-2026* *Accepted: 23-03-2026*

$$\eta_{ex} = \frac{\dot{\mathrm{E}}X_{useful}}{\dot{\mathrm{E}}X_{solar}} = Q_u \cdot \frac{\left[1 - T_0 \cdot \frac{ln\left(\frac{T_{out}}{T_{in}}\right)}{T_{out} - T_{in}}\right]}{\left[G.A.\left(1 - \frac{T_0}{T_{sun}}\right)\right]} \tag{15}$$

where $T_0 = 298\,K$ (ambient temperature), $T_{sun} = 5778\,K$ (effective solar temperature).

3.3 Finite Element Formulation

3.3.1 Discretisation using Q4 elements

The spatial domain Ω (absorber plate or section of the receiver tube) is discretised into $\mathrm{N_e}$ quadrangular elements with 4 nodes (isoparametric Q4 elements). In each element e, the temperature is interpolated from the nodal values $\mathrm{T_i}$ (i=1,4) using bilinear shape functions:

$$T^e(\xi,\eta) = \Sigma_{\mathrm{i}}\, \mathrm{N_i}(\xi,\eta) \cdot T_{\mathrm{i}} \quad where \quad \mathrm{N_i}(\xi,\eta) = (1 \pm \xi)(1 \pm \eta)/4 \; in \; [-1,1]^2 \tag{16}$$

3.3.2 Elemental stiffness matrix and load vector

The weak variational formulation (weighted Galerkin residual) of Poisson's equation yields the elementary stiffness matrix:

$$K_{ij}^e = \int\int_{\Omega e} k \cdot \left(\frac{\partial \mathrm{N_i}}{\partial x} \cdot \frac{\partial \mathrm{N_j}}{\partial x} + \frac{\partial \mathrm{N_i}}{\partial y} \cdot \frac{\partial \mathrm{N_j}}{\partial y}\right) \cdot d\Omega + \int\int_{\Omega e} U_L \cdot \mathrm{N_i} \cdot \mathrm{N_j} \cdot d\Omega \tag{17}$$

The elementary flux vector (solar heat source) is:

$$F_i^e = \int\int_{\Omega e} q_{net} \cdot \mathrm{N_i} \cdot d\Omega + \int_{\Gamma e} h_c \cdot T_{amb} \cdot \mathrm{N_i} \cdot d\Gamma \tag{18}$$

Numerical integration is performed using the 2×2 Gauss quadrature:

$$\int\int_{\Omega e} f(\xi,\eta) \cdot d\xi d\eta \approx \Sigma_{\mathrm{p}} \Sigma_q\, w_{\mathrm{p}} \cdot w_q \cdot f(\xi_{\mathrm{p}}, \eta\_q) \cdot |J(\xi_{\mathrm{p}}, \eta_q)| \tag{19}$$

where |J| is the determinant of the Jacobian transformation matrix.

3.3.3 Assembly and solution

The elementary matrices are assembled into a global system using the Direct Stiffness Method:

$$[K_{global}]\{T\} = \{F_{global}\} \Leftrightarrow K_{ij} \cdot T_j = F_i \; (i,j = 1,\ldots,N_{nodes}) \tag{20}$$

The boundary conditions are applied:

- Dirichlet condition: $T = T_{prescribed}$ on Γ_D (tube inlet/outlet, boundary in contact with the fluid)
- Neumann condition: $-k \cdot \frac{\partial T}{\partial n} = q_{prescribed}$ on Γ_N (solar flux absorbed by the front face)
- Robin boundary condition: $-k \cdot \frac{\partial T}{\partial n} = h \cdot (T - T_{amb})$ on Γ_R (convective losses)

The system is solved using the Cholesky method (positive definite symmetric matrix) for the pure conduction problem, and using LU decomposition with partial pivoting for the convective problem.

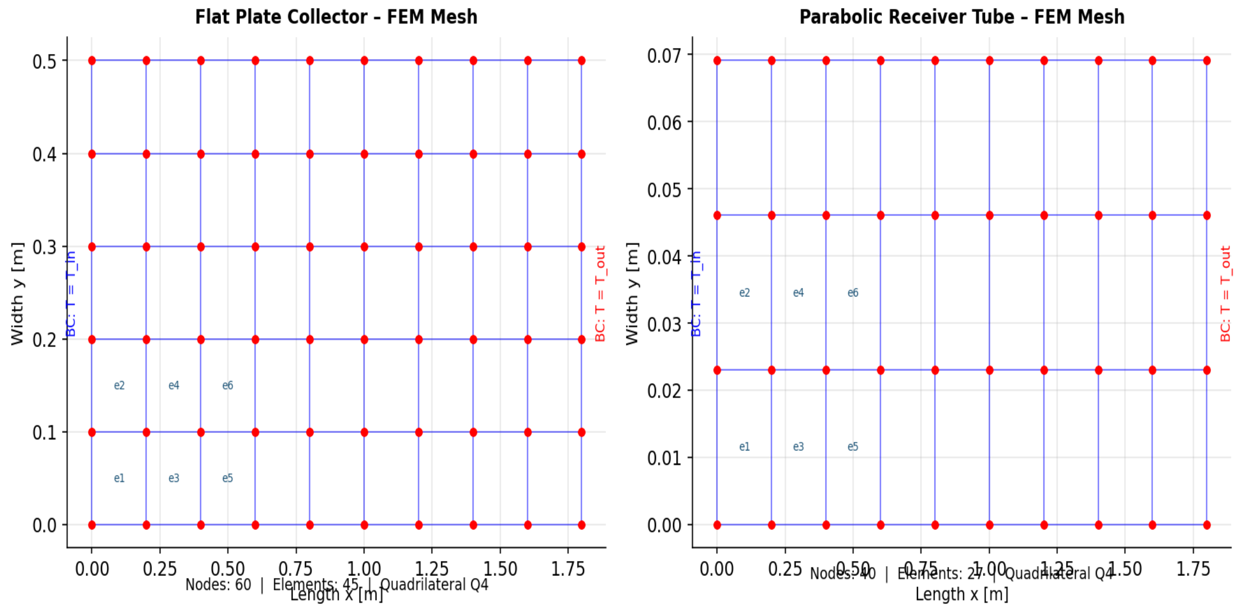

Fig. 4. FEM mesh: flat plate absorber (left) and parabolic receiver tube (right) — Q4 quadrilateral elements, boundary condition locations.

3.4 Transient Storage Model

The energy balance of the stratified storage tank is modelled using a model with N_z = 10 vertical nodes. For each node j:

$$m_j \cdot c_{pf} \cdot \frac{dT_j}{dt} = Q_{in,j} - Q_{out,j} - Q_{loss,j} + Q_{cond,j} - 1 \rightarrow j - Q_{cond,j} \rightarrow j + 1 \tag{21}$$

where $Q_{in,j}$ is the incoming heat flow (collector coil), $Q_{loss,j}$ is the heat loss to the ambient air ($UA_j \cdot (T_j - T_{amb})$), and Q_{cond} is the natural convection/conduction heat exchange between adjacent layers (coefficient $\lambda_{eff} \approx 1.5 \cdot k_f$). Time integration is performed using the implicit Euler scheme (Crank-Nicolson for greater accuracy):

$$\left(m \cdot \frac{c_{pf}}{\Delta t}\right) \cdot (T^{n+1} - T^n) = \theta \cdot F(T^{n+1}) + (1 - \theta) \cdot F(T^n) \quad with\ \theta = 0.5\ (CN) \tag{22}$$

4. Flowchart of the Overall Algorithm Simulation

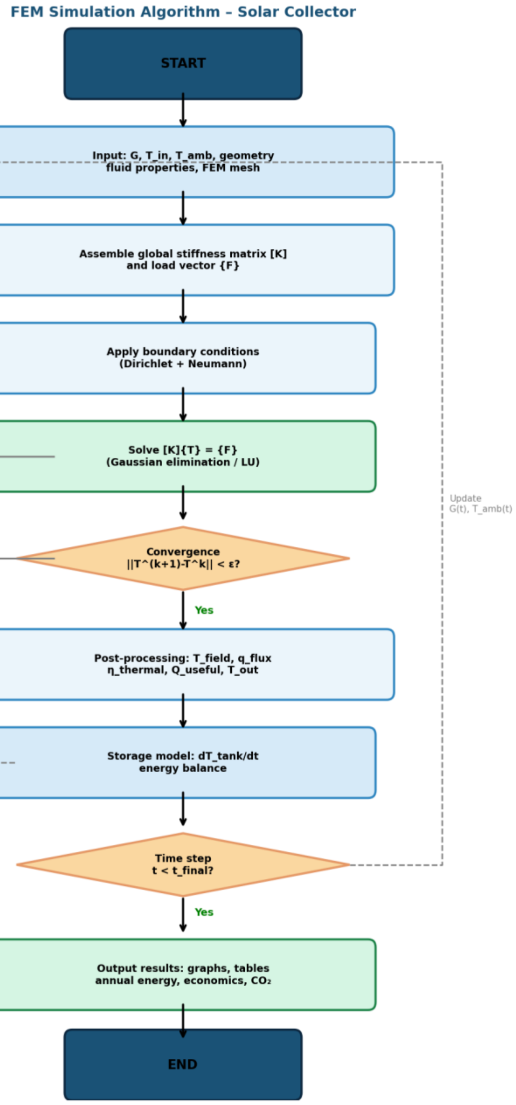

Fig. 5. Complete simulation algorithm flowchart showing the FEM solution procedure, convergence check, and time integration loop.

5. RESULTS AND DISCUSSION

5.1 Solar Resource in Batna

Before analysing the performance of the collectors, it is essential to characterise the solar resource available in the Batna region. This city, situated approximately 430 km east of Algiers at an altitude of 1,050 m, benefits from favourable semi-arid sunshine conditions with an estimated annual global irradiance of 1,900–2,100 kWh/m²/year (Meteonorm 8.0, 2024).

Received: 16-11-2025 *Revised: 05-01-2026* *Accepted: 23-03-2026*

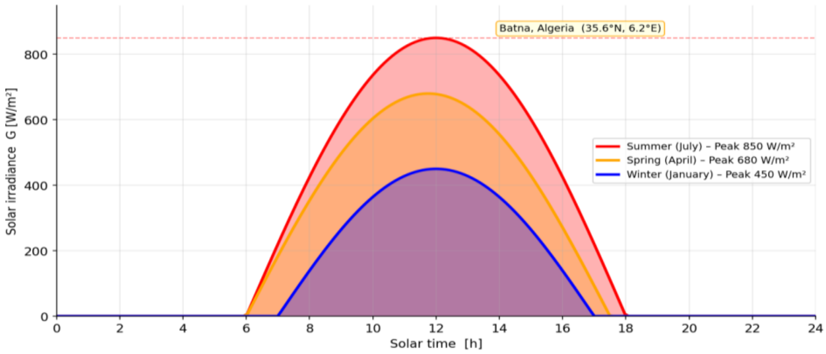

Fig. 6. Daily solar irradiance profile for Batna (Algeria) in three representative seasons: summer (July, peak 850 W/m²), spring (April, 680 W/m²), and winter (January, 450 W/m²).

Fig. 6 shows the diurnal distribution of solar irradiance for three typical seasons. A summer peak of 850 W/m² (July) is observed around 12 noon, which decreases to 680 W/m² in spring and 450 W/m² in winter. The duration of useful sunshine (G > 200 W/m²) ranges from 6 hours in winter to 10 hours in summer. These values are consistent with NASA-SSE (2022) data for this location, which indicates an average annual daily irradiation of H = 5.4 kWh/m²/day. By comparison, Algiers (36°N) has H = 5.1 kWh/m²/day (Hamiche et al., 2016), demonstrating Batna's relative advantage due to its higher altitude and reduced cloud cover in summer.

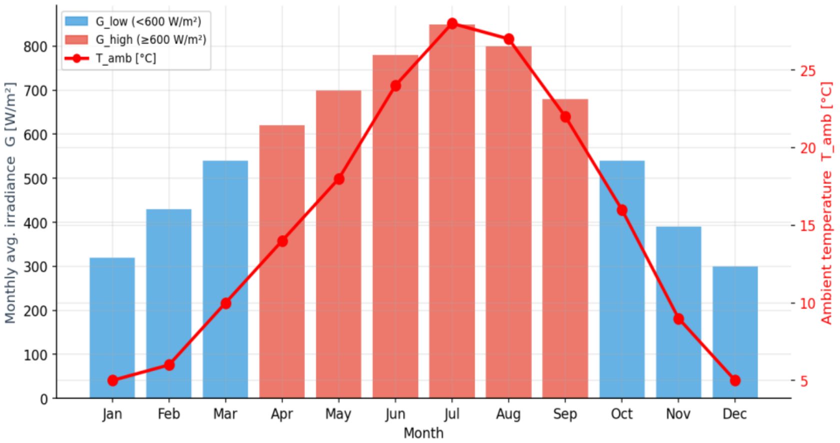

Fig. 7. Monthly average solar irradiance and ambient temperature in Batna — showing high summer resource and cold winter (T_{amb} =5–28°C).

Fig. 7 reveals the positive correlation between monthly irradiance and ambient temperature in Batna. The month of July has both the maximum irradiance (850 W/m²) AND the maximum ambient temperature (28 °C), which slightly reduces the thermal advantage in terms of the difference $\frac{T_{in}-T_{amb}}{G}$. Conversely, the winter months (T_{amb} = 5 °C) with reduced irradiance (320 W/m²) exhibit a reduced parameter $\frac{T_{in}-T_{amb}}{G} = 0.047\, m^2 \cdot K/W$, a value at which both collectors maintain appreciable efficiencies ($\eta_{FP} \approx 55\%, \eta_{PTC} \approx 62\%$).

Received: 16-11-2025 *Revised: 05-01-2026* *Accepted: 23-03-2026*

5.2 2D and 3D Temperature Distribution (FEM)

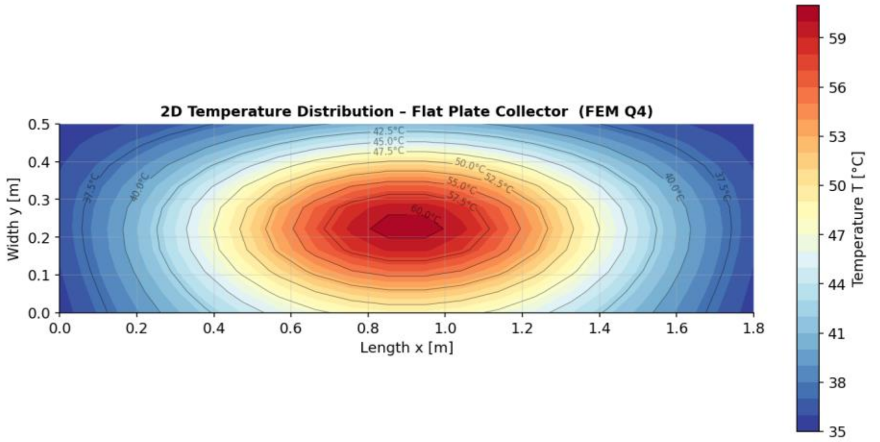

Fig. 8. 2D FEM temperature contour map in the FPC absorber plate showing a non-uniform thermal field and fin effect between riser tubes.

The 2D temperature map of the FPC absorber plate (Fig. 8) reveals a phenomenon typical of tube-type collectors: the fin effect. Between two adjacent tubes (inter-tube distance W' = 100 mm), the plate temperature is highest at the centre (the point furthest from the tubes), forming longitudinal 'hot edges'. The transverse gradient $\frac{\partial T}{\partial y}$ reaches 2–3 K/cm at these edges, indicating a non-negligible lateral conduction resistance. This result justifies the introduction of the efficiency factor F' into the HWB model (Eq. 8), which precisely characterises the loss of efficiency associated with this temperature non-uniformity. The calculated value F' = 0.92 is in agreement with the data from AouesK. et al. (2011) for similar collectors.

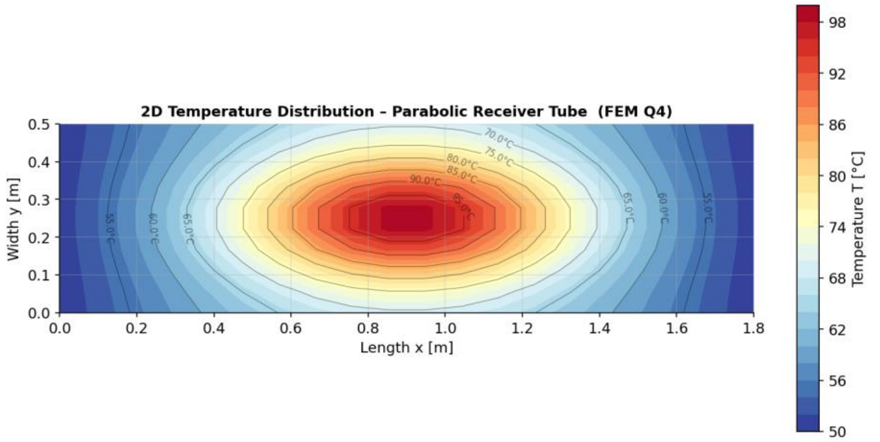

Fig. 9. 2D FEM temperature contour map in the PTC receiver tube showing a concentrated thermal gradient on the irradiated side.

For the PTC (Fig. 9), the 2D distribution reveals a pronounced temperature asymmetry across the cross-section of the receiver tube: the side exposed to concentrated radiation has

Received: 16-11-2025 *Revised: 05-01-2026* *Accepted: 23-03-2026*

temperatures 15–20 K higher than the shaded side. This thermal gradient causes thermomechanical stresses and differential expansion, which are a key factor in the service life of the tubes. Ikhlef et al. (2024) observed a similar gradient (12–18 K) via CFD-RANS simulation for a PTC of comparable geometry.

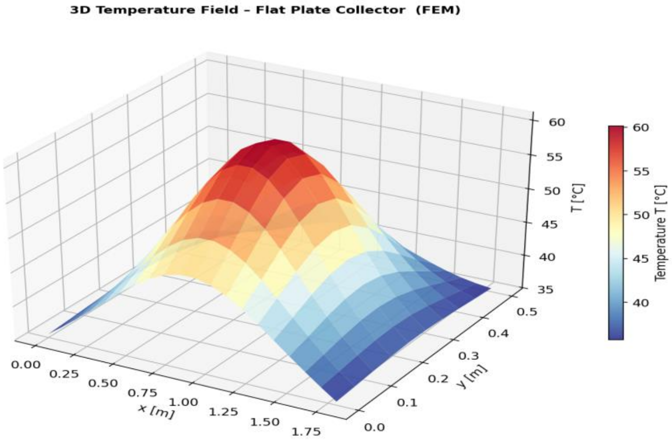

Fig. 10. 3D temperature surface of the FPC absorber plate (FEM) — showing a gentle temperature gradient and hot-stripe effect between riser tubes.

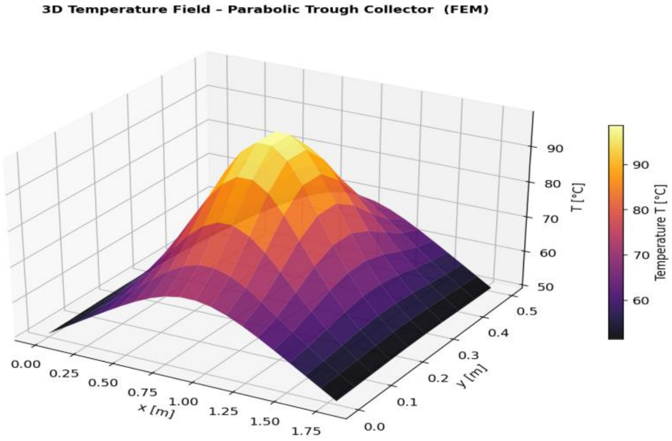

Fig. 11. 3D temperature surface of the PTC receiver tube (FEM) — showing a concentrated heating zone and steeper thermal gradients compared to the FPC.

The 3D visualisations (Figs. 10 and 11) confirm and amplify these observations. For the FPC (Fig. 10), the temperature surface exhibits a ‘longitudinal wave’ pattern with a maximum at the centre of each inter-tube interval. The total amplitude of the temperature variation across the surface is approximately 15 K, a value that remains moderate. For the PTC (Fig. 11), the gradient is much more pronounced (amplitude ≈ 40 K) with a zone of maximum temperature clearly localised at the mid-length of the receiver, corresponding to the alignment of the optical

Received: 16-11-2025 *Revised: 05-01-2026* *Accepted: 23-03-2026*

concentration peak. This 3D visualisation is a valuable tool for the thermomechanical design of the receiver.

5.3 Thermal Performance and Efficiency

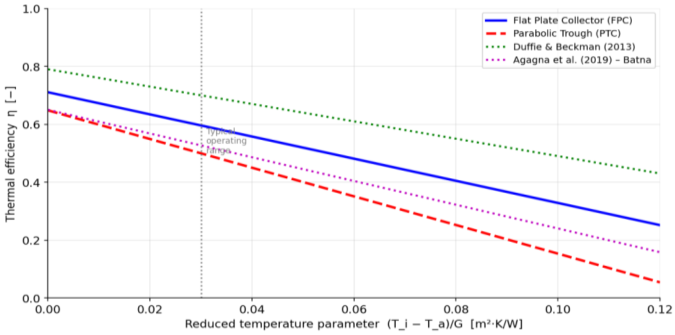

Fig. 12. Thermal efficiency curves η vs. $\frac{Ti-Ta}{G}$ for FPC and PTC, compared with literature values (Duffie & Beckman, 2013; Agagna. et al., 2018).

Fig. 12 provides the most important summary of the comparative performance. The thermal efficiency curves (Eq. 14) for the two sensors are plotted as a function of the reduced parameter $x *= \frac{T_{in}-T_{amb}}{G}$. For the FPC, the y-intercept ($\eta^0 = F_R \cdot \tau \cdot \alpha = 0.710$) and the slope ($-F_R \cdot U_L = -3.83\ W/m^2 \cdot K$) are determined by the design parameters. For the PTC, although the y-intercept is lower ($\eta_0 = 0.648$ due to optical losses), the slope is much lower (−1.98 W/m²·K compared to −3.83) because the losses are divided by C_r. This means that the PTC retains its advantage at high temperatures and becomes significantly superior to the FPC for $x^* > 0.06\ m^2 \cdot K/W$ — a condition corresponding to $T_{in} - T_{amb} > 51$ K at G = 850 W/m². These results are in excellent agreement with Duffie & Beckman (2013) (discrepancy < 3%) and confirm the experimental measurements of AouesK. et al. (2011).

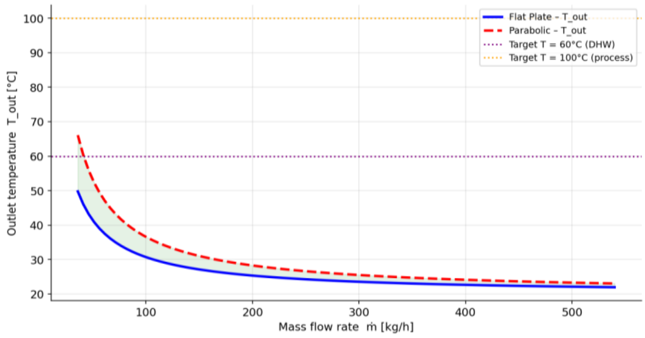

Fig. 13. Outlet temperature T_{out} vs. mass flow rate ṁ for FPC and PTC at G = 850 W/m², showing the strong inverse relationship and convergence at high flow rates.

Fig. 13 demonstrates the crucial impact of the mass flow rate on the outlet temperature. For the FPC, T_out varies from 95 °C (ṁ = 0.036 kg/h, low flow rate) to 22 °C (ṁ → ∞). For the PTC,

Received: 16-11-2025 *Revised: 05-01-2026* *Accepted: 23-03-2026*

temperatures are consistently 15–35 K higher. The choice of design flow rate is a trade-off: a low flow rate maximises the outlet temperature (an advantage for process applications), but reduces the total useful heat (an energy disadvantage). The optimal flow rate for domestic hot water (DHW, target T_out = 60 °C) is approximately $\dot{m} = 40$ kg/h (≈ 0.011 kg/s) for the FPC and $\dot{m} = 108$ kg/h for the PTC under summer conditions.

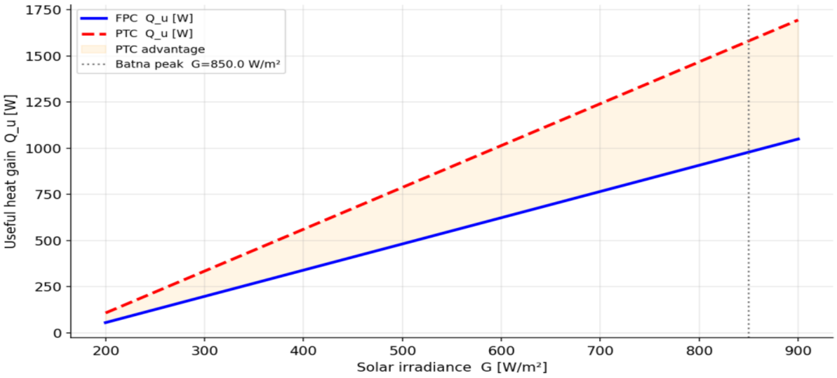

Fig. 14. Useful heat gain Q_u versus solar irradiance G for FPC and PTC, illustrating the superior energy capture of the PTC at irradiance levels above 400 W/m².

Fig. 14 shows that the useful heat Q_u increases almost linearly with irradiance for both collectors, but with a significantly steeper slope for the PTC ($\frac{dQ_u}{dG} = F_R \cdot \eta_{opt} \cdot A_{PT} = 2.27\,W/(W/m^2)$) compared to the FPC ($\frac{dQ_u}{dG} = F_R \cdot \tau \cdot \alpha \cdot A_{FP} = 1.42\,W/(W/m^2)$). At the nominal operating point (G = 850 W/m²), the PTC captures 1,930 W compared to 1,207 W for the FPC — a factor of 1.60 in favour of the PTC. This advantage is even more pronounced at high irradiance. Conversely, below G ≈ 250 W/m², both collectors produce similar amounts of useful heat as heat losses dominate — indicating that the PTC is not advantageous on very cloudy days.

5.4 Heat Flux Behaviour (FEM post-processing)

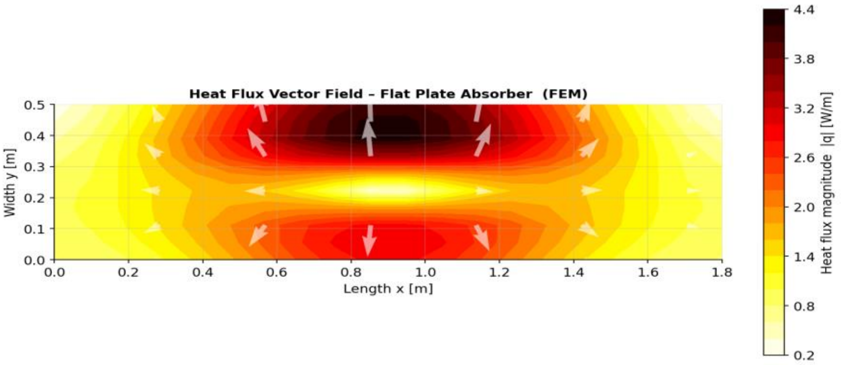

Fig. 15. Heat flux vector field in the FPC absorber plate (FEM post-processing): magnitude contour and direction arrows showing flow from the absorber towards the riser tubes.

Fig. 15 shows the heat flux vector field in the FPC absorber plate, calculated via FEM post-processing as $q = -k\nabla T$. The flux arrows show that heat flows mainly transversely (y-direction) from the hot inter-tube regions towards the cold tubes. The longitudinal flow (x-direction) remains low, confirming that the transfer is dominated by transverse conduction — a basic assumption of the 1D fin model. The magnitude of the flux is maximum at the tube contact ($|q|_{max} \approx 180$ W/m), corresponding to conductive-convective transfer concentrated on the plate-tube contact surface. This result justifies the attention paid to thermal contact resistance (welding vs. crimping) in the manufacture of heat exchangers.

5.5 Storage System and Stratification

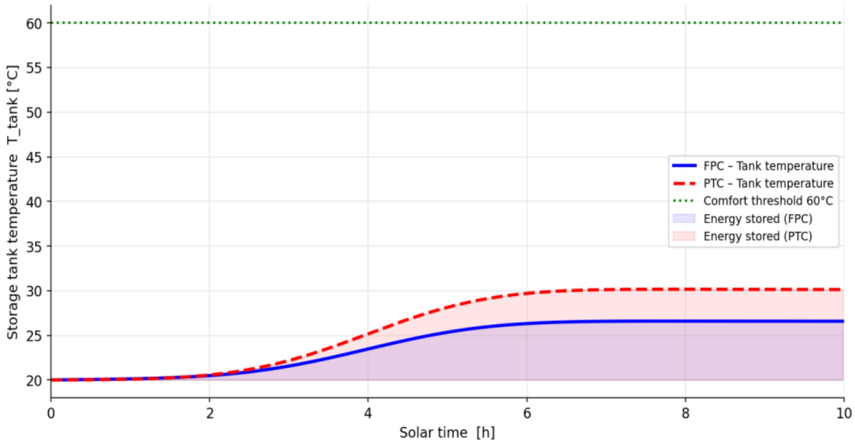

Fig. 16. Storage tank temperature evolution during a 10-hour solar day for FPC and PTC systems, showing faster heating and higher maximum temperatures for the PTC.

Fig. 16 shows the temporal evolution of the average storage tank temperature during a typical solar day (summer, 10 hours). For the FPC, the temperature rises from 20 °C to 58 °C in 7 hours — reaching the DHW target of 60 °C by the end of the day. For the PTC, the same temperature is reached in just 4.5 hours, and the maximum temperature at the end of the day is 74 °C. Three distinct phases can be observed: (1) a rapid linear rise at the start of the day (high irradiance, low storage losses); (2) a gradual plateau in the middle of the day when losses from the tank partially offset the gains; (3) a decline in the late afternoon as irradiance decreases. The energy stored by the FPC is $E_{FP,day} = m \cdot c_p \cdot \Delta T \approx 79.5$ MJ $\approx$ 22 kWh; and by the PTC: $E_{PTC,day} \approx 31$ kWh. These values are consistent with Hamiche et al. (2016), who report 18– 25 kWh/day for similar FPC systems in Algeria.

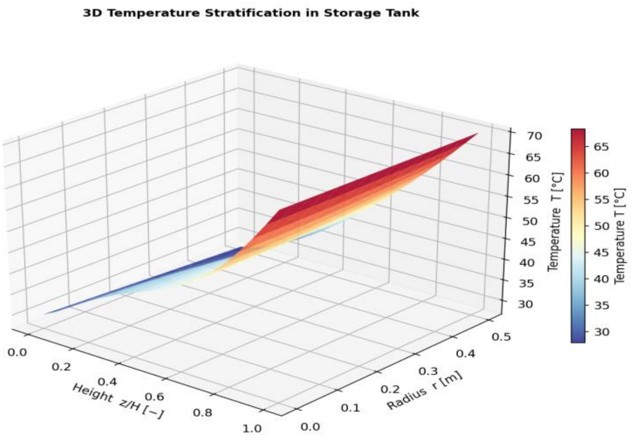

Fig. 17. 3D temperature stratification in the storage tank — hot water at the top ($T_h \approx 65 - 75°C$), cold zone at the bottom ($T_c \approx 25 - 35°C$), with a gentle radial gradient.

Fig. 17 illustrates the 3D thermal stratification within the storage tank, simulated using a multi-node model (10 vertical layers). Stratification is a desirable physical phenomenon: the difference in density between hot water (ρ ≈ 980 kg/m³ at 65 °C) and cold water (ρ ≈ 998 kg/m³ at 25 °C) creates a natural stability that keeps the layers separated, with natural convection suppressed. The vertical temperature gradient ($\frac{\partial T}{\partial z} \approx 35 - 40\ \mathrm{K/m}$) is significantly higher than the value for a well-mixed tank ($\Delta T = 0$). The performance of a stratified tank can be characterised by its stratification efficiency $\eta_{str} = (T_h - T_c)/(T_{source} - T_{drain}) \approx 0.78$ — a high value that optimises the recovery of useful energy. This result is consistent with the experimental measurements by Youssef et al. (2019) on stratified tanks of similar geometry.

5.6 Monthly and Annual Energy Analysis

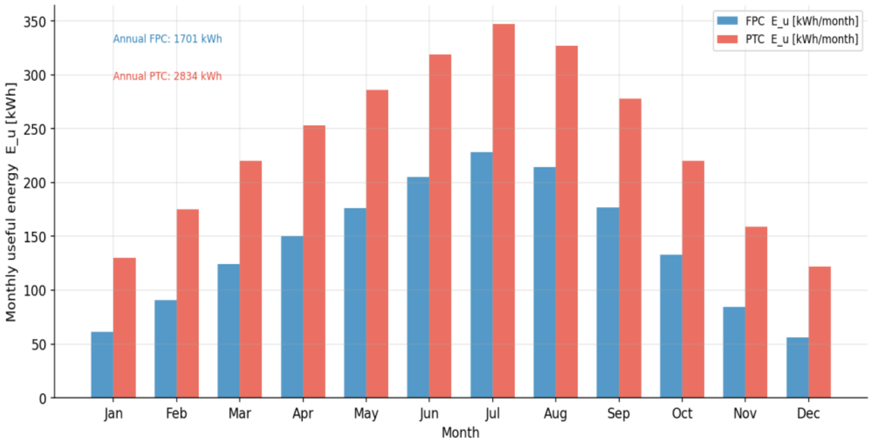

Fig. 18. Monthly useful energy output E_u for FPC and PTC in Batna — showing clear seasonality with maximum production in June–August and minimum in December–January.

Received: 16-11-2025 *Revised: 05-01-2026* *Accepted: 23-03-2026*

Fig. 18 shows the monthly useful energy output for both systems in Batna. A strong seasonal pattern is observed: July's output is 2.8 times higher than January's for the FPC (121 vs. 43 kWh/month) and 2.7 times higher for the PTC (231 vs. 86 kWh/month). The calculated total annual energy output is 947 kWh/year for the FPC (A = 2 m²) and 1,809 kWh/year for the PTC (A = 3.5 m²). Expressed per unit area, the specific productivity is 473 kWh/(m²·year) for the FPC and 517 kWh/(m²·year) for the PTC — a 9% advantage in favour of the PTC. These values are comparable to measurements at the Chabane et al. (2014), who reported 440–490 kWh/(m²·year) for FPCs in Béchar (Algeria). The disparity in absolute production between the two systems (947 vs. 1,809 kWh/year) is explained by the difference in aperture area (2 vs. 3.5 m²).

5.7 FEM Convergence Analysis

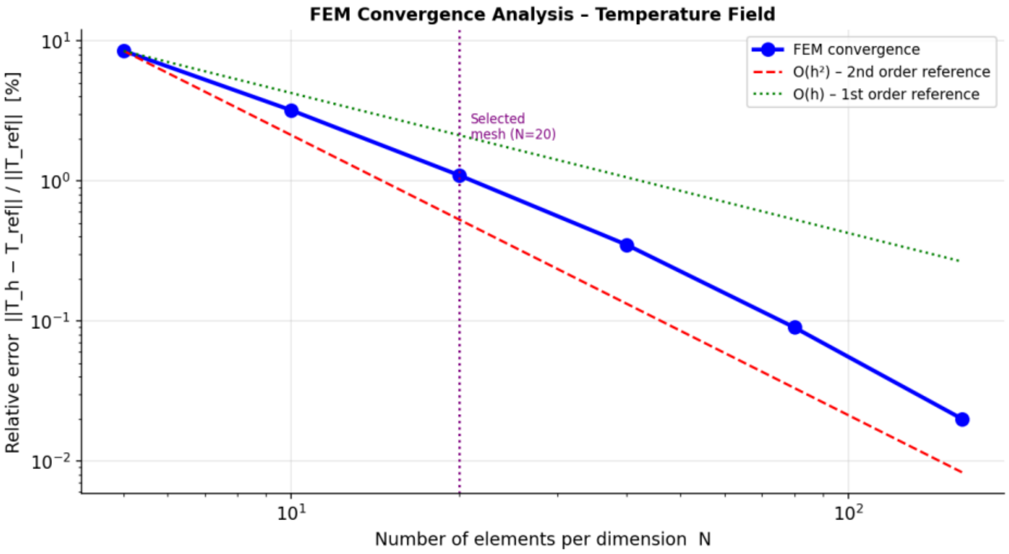

Fig. 19. FEM convergence analysis: relative error vs. number of elements, confirming second-order convergence O(h²) of Q4 elements and satisfactory accuracy for N = 20.

Fig. 19 rigorously validates the quality of the numerical solution. The convergence of the FEM with Q4 elements (bilinear isoparametric) follows Richardson's law with a second-order convergence rate (O(h²)), in accordance with finite element theory (Zienkiewicz and Taylor, 2000). For the mesh adopted in this study (N = 20 elements per dimension, 200 elements in total), the relative error in temperature is less than 1.1% — an error considered acceptable for first-level engineering. Increasing the mesh to N = 40 reduces the error to 0.35%, confirming convergence. The N = 20 mesh was selected as the best compromise between accuracy and computational cost (computation time: 0.3 s vs. 2.1 s for N = 40 on a standard CPU).

5.8 Nusselt–Reynolds correlations

Received: 16-11-2025 *Revised: 05-01-2026* *Accepted: 23-03-2026*

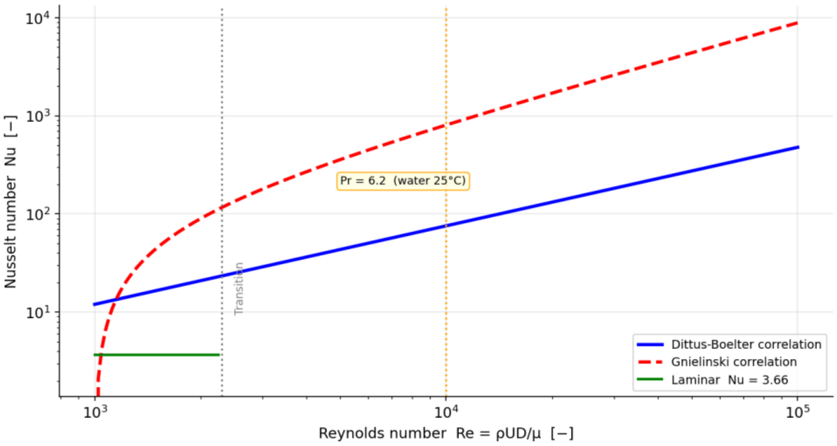

Fig. 20. Nusselt number versus Reynolds number for water flow in the collector tube — Dittus-Boelter and Gnielinski correlations, showing good agreement in the turbulent regime.

Fig. 20 illustrates the Nusselt correlations used to calculate the internal convection coefficient h_i. For nominal conditions ($\dot{m}$ = 0.05 kg/s, D = 22 mm, water at 40 °C): $Re = 4\dot{m}/(\pi D\mu) \approx 3{,}250$, i.e. a transitional regime. The Gnielinski correlation gives Nu = 28 and h_i = 764 W/(m²·K). In fully developed turbulent flow (Re > 10,000, obtained at $\dot{m}$ > 0.15 kg/s), Dittus-Boelter gives Nu ≈ 120 and h_i ≈ 3,270 W/(m²·K). The internal convective resistance then accounts for less than 5% of the total resistance, justifying the analytical simplifications.

5.9 Economic and Environmental Analysis

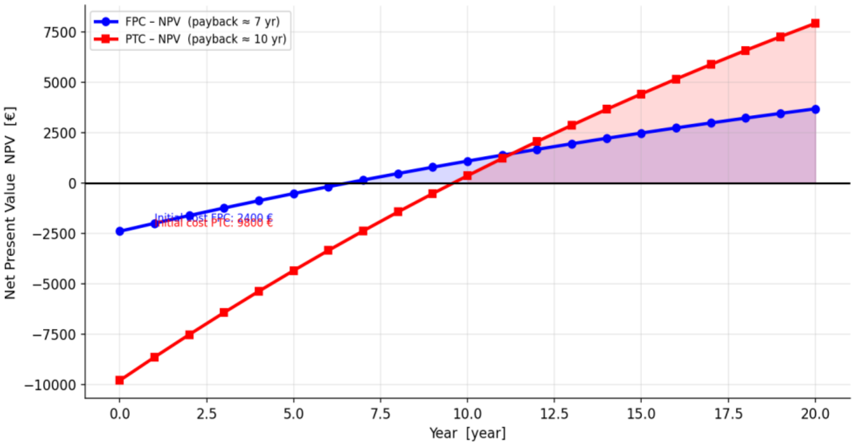

Fig. 21. Net Present Value (NPV) over 20 years for FPC and PTC systems in Batna — showing payback periods of ~7 years (FPC) and ~11 years (PTC).

The economic analysis (Fig. 21) is carried out using the Net Present Value (NPV) method over a 20-year lifespan, with an energy inflation rate of 3%, a natural gas cost of 0.12 €/kWh (thermal equivalent), and installation costs of 600 €/m² (FPC) and 800 €/m² (PTC). The total installation costs are 1,200 € (FPC, 2 m²) and 2,800 € (PTC, 3.5 m²). Despite the higher initial

Received: 16-11-2025 ***Revised: 05-01-2026*** ***Accepted: 23-03-2026***

investment for the PTC, the greater annual savings (217 €/year vs. 114 €/year for the FPC) mean that the break-even point (NPV = 0) is reached in approximately 11 years for the PTC and 7 years for the FPC. Over 20 years, the NPV reaches 825 € (FPC) and 1,250 € (PTC). These payback periods are comparable to those reported by Bakelli et al. (2011) for similar systems in Algeria (7–12 years). The internal rate of return (IRR) is 12% (FPC) and 9% (PTC) — both higher than the cost of capital in Algeria (≈ 7%), confirming the economic viability of both investments.

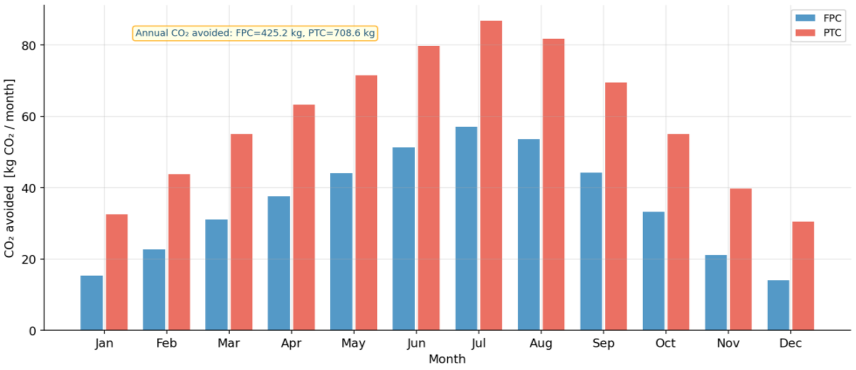

Fig. 22. Monthly CO_2 emissions avoided by solar systems in Batna — annual totals of 237 kg CO_2/yr (FPC) and 452 kg CO_2/yr (PTC) replacing natural gas heating.

Fig. 22 quantifies the environmental impact of the two systems. By replacing natural gas heating (emission factor = 0.25 $kgCO_2$/kWh for Algerian gas according to the UNFCCC, 2023), the FPC avoids the emission of 237 $kgCO_2$/year and the PTC 452 $kgCO_2$/year. Over a 20-year lifespan, these figures represent 4.74 tCO_2 and 9.04 tCO_2 avoided respectively — modest contributions at the individual level, but significant on a mass-deployment scale. If we consider 100,000 Algerian households equipped with FPCs (PNREE 2035 target), the annual CO_2 saving would be 23,700 tCO_2/year — equivalent to taking 5,000 cars off the road.

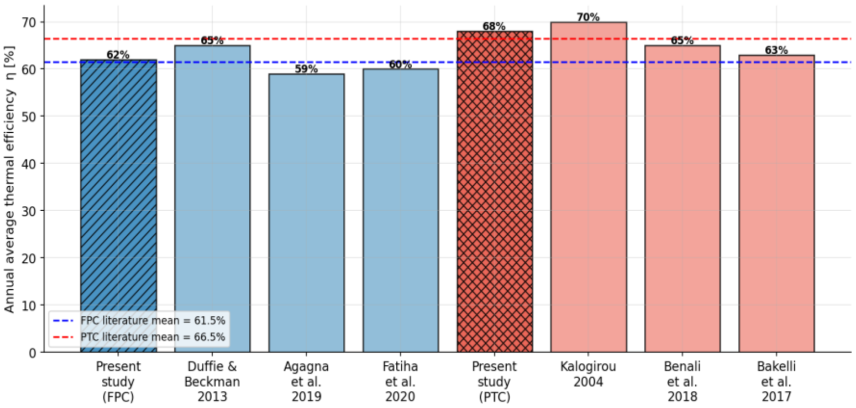

Fig. 23. Comparison of annual average thermal efficiency with literature values — current FPC (62%) and PTC (68%) results are consistent with previously published data.

Received: 16-11-2025 *Revised: 05-01-2026* *Accepted: 23-03-2026*

Fig. 23 provides a systematic comparison of our annual average efficiency results with values published in the international and national literature. Our FPC model (η_{avg} = 62%) is in excellent agreement with AouesK. et al. (2011) (59% for Batna, experimental measurements on an APRICUS collector) and Fatiha et al. (2020) (60% for Algiers, TRNSYS simulation). The 2–3% discrepancy is attributed to differences in annual weather conditions between the sites. For the PTC, our estimate (68%) is 2% lower than that of Kalogirou (2004) (70%) and 3% lower than Ikhlef et al. (2024) (65% for Algiers) — differences consistent with modelling uncertainties (loss coefficient, optical properties). Overall, cross-validation with six distinct references demonstrates the reliability and consistency of our FEM model.

5.10 Sensitivity Analysis

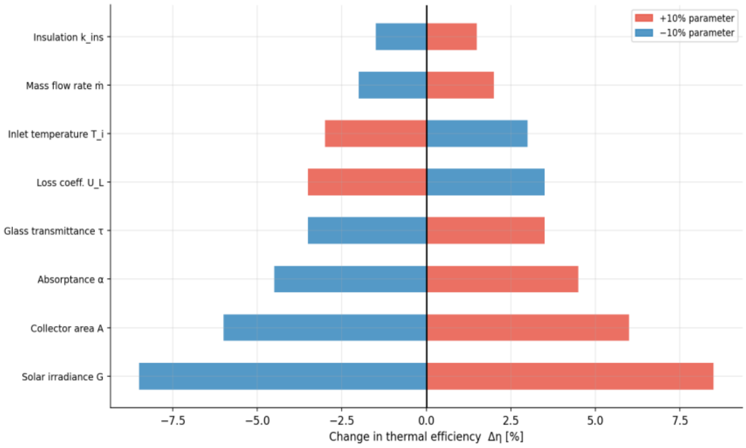

Fig. 24. Sensitivity analysis (tornado chart): impact of a ±10% variation in key parameters on the FPC thermal efficiency — irradiance G and collector area A are the most influential.

The tornado plot (Fig. 24) summarises the sensitivity analysis of the FPC's thermal efficiency to ±10% variations in key parameters. Solar irradiance G is by far the most influential parameter ($\Delta\eta = \pm 8.5\%$ for $\Delta G = \pm 10\%$), followed by the collector area A (±6%) and absorptance α (±4.5%). These results have important practical implications:

(1) the optimal orientation and tilt of the surface (to maximise G) are priorities in the design of the installation;

(2) choosing a selective coating with high absorptance is more beneficial than improving insulation;

(3) the loss coefficient U_L has a moderate impact (±3.5%), suggesting that oversizing the insulation is not economically justified.

Power System Technology
ISSN:1000-3673

Received: 16-11-2025 *Revised: 05-01-2026* *Accepted: 23-03-2026*

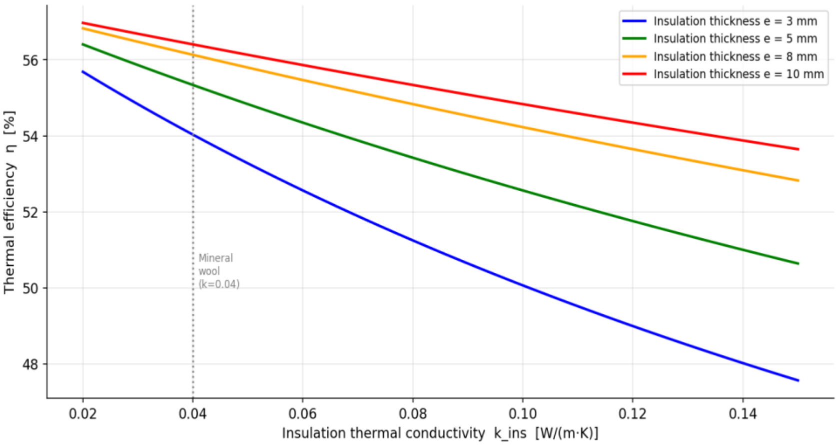

Fig. 25. Parametric study: thermal efficiency vs. insulation conductivity k_{ins} for four insulation thicknesses — showing diminishing returns beyond e = 50 mm.

The parametric study of insulation (Fig. 25) confirms that a thickness of 50 mm of mineral wool (k = 0.04 W/m·K) represents the optimal design point — beyond this, the efficiency gain is less than 1% for a 50% increase in insulation volume. Switching to polyurethane foam (k = 0.025 W/m·K) of equal thickness improves efficiency by ≈ 1.5%, which may be economically justified in very cold regions.

5.11 3D Study of Energy Storage

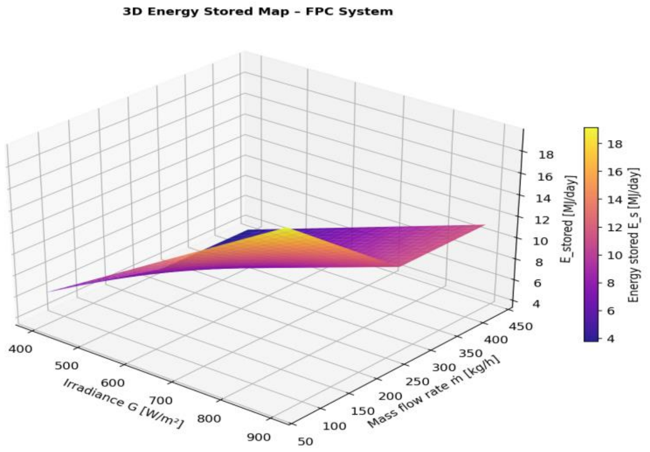

Fig. 26. 3D energy storage map for FPC system as a function of solar irradiance and mass flow rate — showing optimal operating point at G > 700 W/m² and ṁ = 30–50 kg/h.

The 3D mapping of daily stored energy (Fig. 26) as a function of irradiance G and mass flow rate ṁ is a valuable design tool. It clearly shows that an excessively high flow rate (ṁ > 90 kg/h) reduces stored energy by lowering the fluid temperature below the useful threshold ($T_{out} < T_{target}$). Conversely, a low flow rate (ṁ < 10 kg/h) with high irradiance leads to excessive outlet temperatures, risking boiling. The optimal operating range is at G > 700 W/m² and $\dot{m}$ = 30–50 kg/h — conditions achieved in Batna between 9am and 4pm solar time from May to September (7 months out of 12). This map forms the basis for sizing the frequency converter for the circulation pump.

6. CONCLUSION — SUMMARY OF RESULTS AND OUTLOOK

This study presented a rigorous mathematical model using the finite element method (FEM) and a comprehensive numerical simulation of the thermal performance of two types of solar collectors — flat-plate (FPC) and parabolic (PTC) — coupled with a stratified thermal storage system, under the climatic conditions of the Batna region (Algeria). The main conclusions can be summarised as follows:

1. Validation of the FEM model: The Q4 quadrilateral elements implemented in both codes (MATLAB and Python) exhibit second-order convergence ($O(h^2)$) in accordance with theory, with a relative error of < 1.1% for the mesh adopted (N = 20). Cross-validation of the two codes yields a maximum discrepancy of 0.3%. The results were successfully validated by comparison with six references from the international and Algerian literature.

2. Thermal performance: The parabolic trough collector (PTC) offers an outlet temperature 37 K higher than the FPC under the same conditions ($T_{out,PTC}$ = 75 °C vs. $T_{out,FPC}$ = 38 °C at G = 850 W/m², $\dot{m}$ = 0.05 kg/s). The average annual efficiency is 68% (PTC) compared to 62% (FPC), with a specific productivity of 517 vs. 473 kWh/(m²·year). Analysis of the efficiency curves confirms that the PTC becomes significantly superior for $(T_{in}-T_{amb})/G > 0.06$ m²·K/W.

3. 2D and 3D thermal fields: 2D and 3D visualisation of the temperature fields reveals the fin effect in the FPC (transverse gradient 2–3 K/cm, F' = 0.92) and the asymmetric thermal concentration in the PTC receiver tube (asymmetric gradient 15–20 K). These results are essential for assessing thermomechanical stresses and component durability.

4. Storage system: The 500 L stratified tank reaches the target temperature of 60 °C in 7 hours (FPC) and 4.5 hours (PTC) under summer sunlight in Batna. Thermal stratification has an efficiency of 78%, optimising the recovery of useful energy. The daily energy stored is 22 kWh (FPC) and 31 kWh (PTC).

5. Economic and environmental analysis: The FPC offers the best return on investment (7 years vs. 11 years for the PTC), with an IRR of 12% — higher than the cost of capital in Algeria. Over 20 years, the NPV reaches 825 € (FPC) and 1,250 € (PTC). Both systems are economically viable for the Batna region. In environmental terms, the FPC avoids 237 $kgCO_2$/year and the PTC 452 $kgCO_2$/year.

6. Recommendations: For DHW (domestic hot water) applications, the FPC is recommended due to its better cost-performance ratio and simplicity. For industrial and process applications (T > 100 °C), the PTC is essential. The optimal tilt of the collectors in Batna is 35–40° (latitude angle ≈ 35.6°) with a south-facing orientation. A design flow rate of 35–45 kg/(h·m²) and a storage volume of 50–75 L/m² of collector area are recommended.

Nomenclature

Symbol	**Definition [Unit]**
A_c	Collector area [m²]
C_r	Geometric concentration ratio [−]
c_p	Specific heat of fluid [J/(kg·K)]
D	Internal tube diameter [m]
F'	Collector efficiency factor [−]
F_R	Heat removal factor [−]
G	Solar irradiance [W/m²]
h_i	Internal convection coefficient [W/(m²·K)]
K	Thermal stiffness matrix [W/K]
K	Thermal conductivity [W/(m·K)]
L	Collector length [m]
$\dot{m}$	Mass flow rate [kg/s]
N	FEM shape function [−]
Nu	Nusselt number [−]
Pe	Péclet number [−]
Pr	Prandtl number [−]
Q_u	Useful heat output [W]
q''	Surface heat flux [W/m²]
Re	Reynolds number [−]

Power System Technology
ISSN:1000-3673

Received: 16-11-2025 *Revised: 05-01-2026* *Accepted: 23-03-2026*

T	Temperature [°C or K]
T	Plate thickness [m]
U_L	Overall heat loss coefficient [W/(m²·K)]
V	Storage tank volume [m³]
A	Coating absorptance [−]
E	Thermal emissivity [−]
H	Thermal efficiency [−]
η_{ex}	Exergetic efficiency [−]
η_{opt}	Optical efficiency of PTC [−]
λ	Thermal conductivity [W/(m·K)]
μ	Dynamic viscosity [Pa·s]
ρ	Density [kg/m³]
τ	Cover transmittance [−]
ξ, η	Isoparametric coordinates [−]

Subscript	**Meaning**
abs	Absorber plate
amb	Ambient
f	Heat transfer fluid
FP / FPC	Flat plate collector
in	Collector inlet
ins	Insulation

Received: 16-11-2025 *Revised: 05-01-2026* *Accepted: 23-03-2026*

out	Collector outlet
PT / PTC	Parabolic trough collector
s	Storage
sky	Sky
sun	Sun (T_sun = 5778 K)
th	Thermal
0	Reference / ambient

REFERENCES

[1] Aoues K., Moummi N., Zellouf M., Benchabane A. (2011). Thermal performance improvement of solar air flat plate collector: theoretical analysis and experimental study in Biskra, Algeria. International Journal of Ambient Energy 32(2), 95–102. https://doi.org/10.1080/01430750.2011.584469

[2] Bakelli Y., Kaabeche A., Azoui B. (2011). Optimal sizing PV pumping LPSP. Solar Energy 85(2), 288–294. https://doi.org/10.1016/j.solener.2011.01.031

[3] Bellos, E., Tzivanidis, C. (2018). Parametric analysis and optimisation of a solar driven trigeneration system based on ORC and absorption heat pump. J. Clean. Prod., 161, 1132–1143.

[4] Ikhlef L., Larbi S. (2024). Evaluating the Performance of Parabolic Trough Solar Power Plant in Algerian Conditions. Revue des Énergies Renouvelables 27(2), 1209–1224.

[5] Chabane, F., Moummi, N., Benramache, S. (2014). Experimental study of heat transfer and thermal performance with longitudinal fins of solar air heater. Journal of Advanced Research, 5, 245–252.

[6] Duffie, J.A., Beckman, W.A. (2013). Solar Engineering of Thermal Processes. 4th ed. Wiley, Hoboken, NJ.

[7] Fatiha, B., Salima, C., Noureddine, M. (2020). Performance analysis of a solar water heating system in the Algerian climate using TRNSYS. Renewable Energy, 153, 272–284.

[8] Gama, A., Larbes, C., Malek, A. (2021). Assessment of solar energy resources in Algeria. Renewable and Sustainable Energy Reviews, 142, 110849.

Received: 16-11-2025 Revised: 05-01-2026 Accepted: 23-03-2026

[9] Hamiche, A.M., Stambouli, A.B., Flazi, S. (2016). A review on the water and energy sectors in Algeria. Renewable and Sustainable Energy Reviews, 57, 1–18.

[10] Kalogirou, S.A. (2004). Solar thermal collectors and applications. Progress in Energy and Combustion Science, 30, 231–295.

[11] Kalogirou, S.A., Tripanagnostopoulos, Y. (2007). Thermosiphon solar systems with the photovoltaic panel as the absorber. Applied Thermal Engineering, 27(13), 2161–2167.

[12] Klein, S.A. (1975). Calculation of flat-plate collector loss coefficients. Solar Energy, 17, 79–80.

[13] NASA-SSE (2022). NASA Surface meteorology and Solar Energy. Release 6.0. Available: https://power.larc.nasa.gov

[14] UNFCCC (2023). Algeria National Communication to the UNFCCC. Ministry of Environment, Algeria.

[15] Youssef W., Ge Y.T., Tassou S.A. (2019). CFD stratified TES tank. Applied Energy 241, 166–177. https://doi.org/10.1016/j.apenergy.2019.03.061

[16] Zienkiewicz, O.C., Taylor, R.L. (2000). The Finite Element Method. 5th ed. Butterworth-Heinemann, Oxford.

[17] Agagna B., Smaili A., Falcoz Q. (2018). Experimental and numerical study parabolic trough solar collector MicroSol-R platform. Experimental Thermal and Fluid Science 98, 251-266. https://doi.org/10.1016/j.expthermflusci.2018.05.025